Magnetic instability in a dilute circular rarefaction wave

Dieckmann, M. E., Sarri, G., & Borghesi, M. (2012). Magnetic instability in a dilute circular rarefaction wave. *Physics of Plasmas*, *19*(12), -. [122102]. https://doi.org/10.1063/1.4769128

Magnetic instability in a dilute circular rarefaction wave

M. E. Dieckmann, G. Sarri, and M. Borghesi

Citation: Phys. Plasmas **19**, 122102 (2012); doi: 10.1063/1.4769128
View online: http://dx.doi.org/10.1063/1.4769128
View Table of Contents: http://pop.aip.org/resource/1/PHPAEN/v19/i12
Published by the American Institute of Physics.

Magnetic instability in a dilute circular rarefaction wave

M. E. Dieckmann,[1,a)] G. Sarri,[2] and M. Borghesi[2]
[1]Department of Science and Technology (ITN), Linkoping University, 60174 Norrkoping, Sweden
[2]Centre for Plasma Physics, School of Mathematics and Physics, Queen's University of Belfast, Belfast BT7 1NN, United Kingdom

(Received 8 October 2012; accepted 13 November 2012; published online 4 December 2012)

The growth of magnetic fields in the density gradient of a rarefaction wave has been observed in simulations and in laboratory experiments. The thermal anisotropy of the electrons, which gives rise to the magnetic instability, is maintained by the ambipolar electric field. This simple mechanism could be important for the magnetic field amplification in astrophysical jets or in the interstellar medium ahead of supernova remnant shocks. The acceleration of protons and the generation of a magnetic field by the rarefaction wave, which is fed by an expanding circular plasma cloud, is examined here in form of a 2D particle-in-cell simulation. The core of the plasma cloud is modeled by immobile charges, and the mobile protons form a small ring close to the cloud's surface. The number density of mobile protons is thus less than that of the electrons. The protons of the rarefaction wave are accelerated to 1/10 of the electron thermal speed, and the acceleration results in a thermal anisotropy of the electron distribution in the entire plasma cloud. The instability in the rarefaction wave is outrun by a TM wave, which grows in the dense core distribution, and its magnetic field expands into the rarefaction wave. This expansion drives a secondary TE wave. © *2012 American Institute of Physics*. [http://dx.doi.org/10.1063/1.4769128]

I. INTRODUCTION

Magnetic instabilities in expanding plasmas or in density gradients are of interest for laser fusion, where magnetic fields can reduce the particle's mobility,[1] and for astrophysical plasmas, where they can generate magnetic fields from noise levels. Magnetic field generation in the interstellar medium (ISM)[2] by the interplay of the electrons of the hot ionized medium with the spatially nonuniform (ISM) plasma or the amplification of magnetic fields in the turbulent plasma close to supernova remnant (SNR) shocks[3–5] are examples.

The growth of magnetic fields in rarefaction waves on an electron timescale[6–9] has recently been observed experimentally[10] and with particle-in-cell (PIC) simulations.[7,11] The instability is driven by a thermal anisotropy of a single electron distribution rather than by counterstreaming electron beams[12] and is thus similar to the Weibel instability in its original form.[13–17] It is the result of the electron's slowdown by the ambipolar electrostatic field, which is sustained by the plasma density gradient of the rarefaction wave. This electrostatic field counteracts the charge separation along the plasma density gradient that arises from the difference in the thermal speeds of electrons and ions. It accelerates the ions and slows down the electrons along this direction, which generates the thermal anisotropy.

Previous simulations[6,7,11] have considered systems, in which hot electrons accelerate an equal number of initially cold ions. Here, the acceleration of protons, which are distributed in form of a hollow ring, by the ambipolar electrostatic field is examined with a PIC simulation. This proton ring distribution is a good approximation of the cross section of the ions of a laser-heated wire, as long as it is located far away from the laser impact point.

The ablation of the wire and the resulting magnetic instabilities have been examined experimentally in Ref. 10. The wire in the experiment is composed of heavy ions, which can not be accelerated to high speeds by the expanding electrons. The light protons that feed the rarefaction wave originate from surface impurities and they are approximated here by the hollow ring distribution. The low number of mobile protons dilutes the rarefaction wave. This is also observed in the experiment where its number density is $\sim 10^{18}\mathrm{cm}^{-3}$,[10] which is well below the solid ion number density. The electrons have the temperature 32 keV and are spatially uniform within the plasma cloud, while the electrons in the experiment have MeV energies and are confined to the wire's surface.[18] The initial conditions of the simulation are thus not an exact representation of the experimental conditions. Reducing the electron temperature and distributing the electrons over a wide interval is computationally efficient, and it ensures that the overall thermal energies in the experiment and simulation are comparable.

The purpose of our simulation is threefold. We want to determine if the gradient-driven magnetic instability always develops in the rarefaction wave or if competing instabilities can outrun it. Second, we want to determine if the lower proton density results in a weaker thermal anisotropy of the electrons and, third, if and how the expansion of the dilute rarefaction wave differs from the dense one in Ref. 11.

Our results are as follows. The protons at the front of the dilute rarefaction wave are accelerated to about the same speed within the same time interval as those in the dense one in Ref. 11. This confirms our expectation. The electrostatic potential of the plasma with respect to the surrounding vacuum is fully determined by the thermal pressure of the electrons, which is the same here and in our simulation in Ref. 11. The stronger reduction of the electron's thermal

a)Electronic mail: Mark.E.Dieckmann@itn.liu.se.

energy in Ref. 11 compared to the one here does not lead to detectable differences in the plasma expansion. The same magnitude of the electrostatic potential and the therefrom resulting equal deceleration of the electrons in the direction of the density gradient imply that the electron's thermal anisotropies here and in Ref. 11 are equally strong. However, the much lower electron number density in the rarefaction wave we model here delays the onset of the gradient-driven magnetic instability. It develops instead in the dense core of the plasma cloud and the strong magnetic fields diffuse out into the rarefaction wave.

The magnetic fields grow in the radial interval of the plasma cloud in which the temperature anisotropy and the number density of the electrons are large. The magnetic field source is thus a Weibel-type instability and not the competing thermoelectric instability.[19] The latter is inefficient in our case study, because the electron density gradient is aligned with the electron temperature gradient and because the expanding rarefaction wave is circularly symmetric.

We also observe here the same secondary magnetic instability as in Ref. 11, which yields the growth of in-plane magnetic fields. Our present simulation setup confines the secondary wave in the plasma cloud's core, while it developed in the expanding rarefaction wave in Ref. 11. This confinement simplifies the interpretation of the data. Our results suggest that the in-plane magnetic fields are generated by a mode conversion of a transverse-magnetic (TM) wave into a transverse-electric (TE) wave. This is a well-known process in waveguides with a variable cross section, which are important in antenna theory.[20] The variable cross section is here the result of the proton expansion.

The structure of this paper is as follows. The PIC simulation scheme and the initial conditions are summarized in Sec. II. Section III presents the simulation results, which are discussed in Sec. IV.

II. THE SIMULATION CODE AND THE INITIAL CONDITIONS

A PIC code approximates a plasma by an ensemble of computational particles (CPs) and it uses their collective charge distribution $\rho(\mathbf{x})$ and current distribution $\mathbf{J}(\mathbf{x})$ to evolve in time the electromagnetic fields on a spatial grid. The electric $\mathbf{E}$ and magnetic $\mathbf{B}$ fields update in turn the momentum of each CP through the relativistic Lorentz force equation. The PIC scheme is discussed in detail in Ref. 21.

Most codes evolve the electromagnetic fields through the discretized forms of the Ampére's and Faraday's laws

$$\frac{\partial \mathbf{E}}{\partial t} = \frac{1}{(\mu_0 \epsilon_0)} \nabla \times \mathbf{B} - \frac{1}{\epsilon_0} \mathbf{J}, \tag{1}$$

$$\frac{\partial \mathbf{B}}{\partial t} = -\nabla \times \mathbf{E}, \tag{2}$$

and they fullfill Gauss' law $\nabla \cdot \mathbf{E} = \rho/\epsilon_0$ and $\nabla \cdot \mathbf{B} = 0$ either as constraints or through correction steps. The relativistic Lorentz force equation

$$\frac{d\mathbf{p}_j}{dt} = q_i[\mathbf{E}(\mathbf{x}_j) + \mathbf{v}_j \times \mathbf{B}(\mathbf{x}_j)] \tag{3}$$

is used to update the momentum $\mathbf{p}_j$ of the jth particle of species i. The collective behavior of the ensemble of the CPs of species i approximates well that of a plasma species, provided that the charge-to-mass ratio of the plasma particles equals the ratio q_i/m_i of the CPs, that the plasma is collisionless and that the statistical representation of the computational plasma is adequate. We use the numerical scheme discussed in Ref. 22.

Our initial conditions and their connection to the experiment are visualized in Fig. 1. The axis of the wire on the left hand side is parallel to $\mathbf{z}$. The simulation resolves a cross-section of this wire in the x-y plane with an origin $x = 0$, $y = 0$ in the center of the wire. This cross-section has a z-coordinate that is sufficiently far away from that of the laser impact point, so that we do not have to model the laser pulse in the simulation.

In the experiment, the hot electrons stream uniformly from the laser impact point along the wire's surface[18] to the cross section that corresponds to our simulation plane. We thus approximate the wire's cross section by the circular plasma cloud shown on the right hand side of Fig. 1. Hot electrons fill the entire cross section of the plasma cloud with radius $r = r_W$. Their spatially uniform number density n_0 within the cloud gives the plasma frequency ω_p. The mobile protons fill a hollow ring with the outer radius $r = r_W$ and with the inner radius $r = 0.95 r_W$. The interior $r < 0.95 r_W$ of the hollow ring contains an immobile positive charge background. The charge density of the electrons equals at any location x, y with $x^2 + y^2 < r^2$ that of the positive charge carriers and the mean speeds of both mobile species are zero. No net charge and no net current are initially present. All initial electromagnetic fields are thus set to zero. The cloud is immersed in a vacuum, and the boundary conditions of the simulation box are periodic.

The outer cloud radius $r_W = 14.2\lambda_e$, where $\lambda_e = c/\omega_p$ is the electron skin depth within the cloud. The temperature of the relativistic Maxwellian distribution that represents the electrons is 32 keV and their thermal speed is $v_e = c/4$. This relativistic Maxwell-Jüttner distribution is $f(p) = (4\pi m^3 c^3 \theta \tilde{K}_2(1/\theta))^{-1} \exp(-\gamma(p)/\theta)$ with $\gamma(p) = (1 + (p/mc)^2)^{1/2}$, $\theta = kT/mc^2$ and the modified Bessel function of the second kind $\tilde{K}_2(\theta)$. The bulk of the electrons thus moves at nonrelativistic speeds, which allows us to easily decompose their

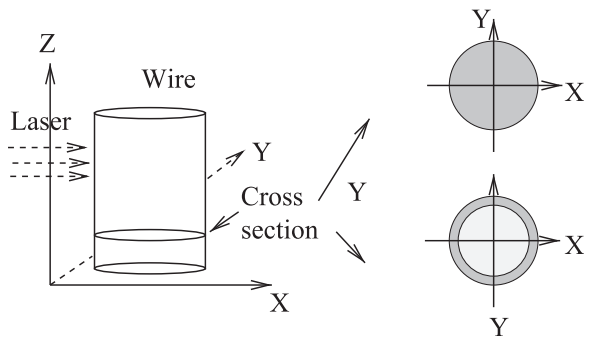

FIG. 1. The initial conditions: The experimental setup is shown to the left, where we assume that a long wire is aligned with z. The initial electron distribution in the simulation is shown to the upper right and the proton ring distribution (dark gray shade) and the positively charged immobile background (light gray shade) to the lower right.

radial and azimuthal velocity components. The electron Debye length $\lambda_d = v_e/\omega_p$ equals $5.6\Delta_x$, where Δ_x is the side length of a quadratic grid cell. We use the correct mass ratio between the electrons and the protons in the ring distribution. The proton temperature is 10 eV and their thermal speed $v_p = 3.1 \times 10^4$ m/s. The Maxwell-Jüttner distribution we use also to initialize the initial speeds of the computational ions practically equals a Maxwell velocity distribution due to the nonrelativistic ion speeds.

The quadratic area $L \times L$ of the 2D simulation box with the side length $L = 75.5\lambda_e$ is resolved by $N_g = 1700$ grid cells in the x and y directions. We represent the electrons by $N_e = 8 \times 10^8$ CPs and the protons by $N_p = N_e$ particles. Since the protons occupy a smaller volume, their numerical weight is lower. A time interval $t\omega_p = 800$ is resolved. We normalize time to ω_p, space to the initial cloud radius r_W, and the electron and proton velocities to their respective initial thermal speeds v_e and v_p. The electric and magnetic fields are normalized to $m_e\omega_p c/e$ and $m_e\omega_p/e$, respectively.

III. SIMULATION RESULTS

The kinetic energy of electrons with the mass m_1 is $K_1(t) = m_1c^2\sum_{j=1}^{N_e}[\Gamma_j - 1]$, where the summation is over all computational electrons with the Lorentz factors Γ_j and $K_0 \equiv K_1(0)$. The kinetic energy of the mobile protons with mass m_2 is $K_2(t) = m_2c^2\sum_{j=1}^{N_p}[\Gamma_j - 1]$. We use the relativistic expression of the proton kinetic energy the code is solving for even though they do not reach a relativistic speed. The charge-to-mass ratio of the computational electrons is 1836 times larger than that of the protons. The energy of the in-plane electric field is $E_{E\perp}(t) = (\Delta_x^3/2\epsilon_0)\sum_{i,j=1}^{N_g} E_p^2(i.j.t)$, where $E_p(i,j,t) = [E_x^2(i,j,t) + E_y^2(i,j,t)]^{1/2}$. The energy density of the out-of-plane magnetic field $E_{Bz}(t) = (\Delta_x^3/2\mu_0)\sum_{i,j=1}^{N_g} B_z^2(i.j.t)$.

Figure 2 shows their time evolution. The electrons sustain a rapid energy loss during $0 < t < 20$. This energy is transferred to the ambipolar electric field, which grows and saturates during this time. This field accelerates the protons and the electrons have transferred about 10% of their initial energy to them at $t = 800$. The initial oscillations of $E_{E\perp}$ have damped out at $t \approx 200$ and $E_{E\perp}$ reaches a steady state value of $\approx 10^{-2}K_0$. E_{Bz} grows initially slowly. The faster growth of the magnetic energy in the time interval $400 < t < 700$ is followed by its saturation. The magnetic energy remains well below that found in Ref. 11 and about two orders of magnitude below the electric one. We will examine now in more detail the field and particle distributions at the time $t = 27$ when the electrostatic field reaches its peak value, at $t = 500$ when the magnetic field grows fastest and at $t = 800$ when the magnetic field saturates.

A. Early time t = 27

The modulus of the in-plane electric field at $t = 27$ is shown in Fig. 3. The electric field has the expected circular symmetry. It peaks at $r \approx r_W$. It gradually decreases for increasing values of r and reaches noise levels at $r \approx 2r_W$. Circular electric field oscillations are visible in the cloud's core $r < r_W$. Since the positive charged background is immobile in this region, these electrostatic waves must be Langmuir waves. The magnetic field remains at noise levels at this time (not shown).

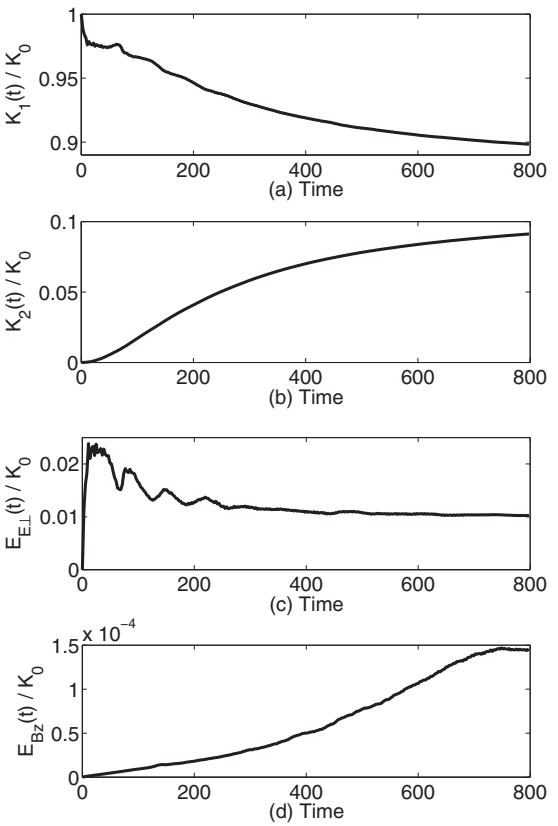

FIG. 2. Energy densities in units of the initial electron thermal energy: The electron energy (a), the proton energy (b), the energy density of the in-plane electric field, (c) and of the out-of-plane magnetic field (d).

The phase space density distributions $f_e(r, v_r)$ and $f_p(r, v_r)$ of electrons and protons, which are functions of the radius $r = (x^2 + y^2)^{1/2}$ and of the radial velocity component $v_r = (v_x^2 + v_y^2)^{1/2}$, are displayed in Fig. 4. They are derived as follows. The circular symmetry of the cloud and the energy exchange between electrons (s = e) and the mobile protons (s = p), which is at least initially limited to the x,y-plane and a function of the radius, imply that distributions

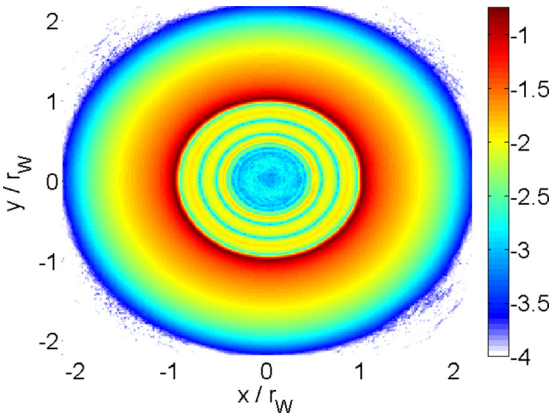

FIG. 3. The 10-logarithmic modulus of the electric field $|E_p(x, y)|$ sampled at the time $t = 27$ (enhanced online) [URL: http://dx.doi.org/10.1063/1.4769128.1].

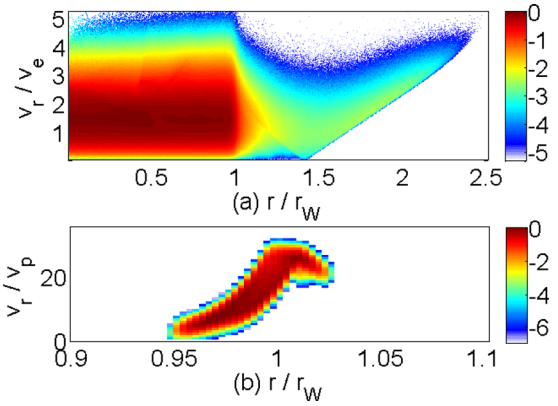

FIG. 4. The 10-logarithmic phase space densities $f_e(r, v_r)$ of the electrons (a) and $f_p(r, v_r)$ of the protons (b). The densities are normalized to their initial value. The simulation time is $t = 27$ (enhanced online) [URL: http://dx.doi.org/10.1063/1.4769128.2].

$\hat{f}_s(r, v_r, v_z)$ will develop for both species. We neglect the v_z direction and define the average over the azimuthal angle ρ

$$f_s(r, v_r) = (2\pi r)^{-1} \int_{\rho=0}^{2\pi} \hat{f}_s(r, v_r) r d\rho, \tag{4}$$

which greatly improves the visualized dynamical range of the phase space densities. We normalize $f_s(r, v_r)$ by its maximum value at $t = 0$. The resulting phase space densities are thus constant as a function of r at $t = 0$ within the radial interval the mobile species occupy.

The protons have been accelerated to several times v_p at $t = 27$ and their mean speed increases with r. The protons have, however, not moved far beyond r_W during this short time. The fastest electrons have reached a radius $r \approx 2.3 r_W$. Their density profile shows a straight line from $r \approx 1.5 r_W$ and $v_r \approx 0$ to $r \approx 2.3 r_W$ and $v_r \approx 4$. These are the electrons that have escaped from the cloud before the ambipolar electric field has fully developed. The linear density profile simply reflects that faster electrons have propagated to larger radii during $t = 27$. The ambipolar electric field, which has been built up after the first electrons escaped into the vacuum (see Fig. 2(c)), affects the electrons at lower r, and we can observe a decrease of the peak electron speed as we go from $r \approx 2.3 r_W$ to $r \approx 1.5 r_W$. The electrons lose kinetic energy as they overcome the electrostatic ambipolar potential. This potential is also responsible for the drastic drop of the electron number density at $r \approx r_W$. It is evident from Fig. 4 that the electron charge for $r > 1.03 r_W$ is not compensated by a proton charge. The electric field at $r > 1.03 r_W$ in Fig. 3 is thus sustained by the electron sheath.

The online enhancement of Fig. 4 shows that the electrons cross the simulation box boundary shortly after $t = 27$. Their low number density implies that the electron two-stream instability does not develop during the simulation time due to a low growth rate. The electrons are accelerated by the electrostatic field of the rarefaction wave as they re-enter the plasma cloud. The low number density of these accelerated electrons implies again that no plasma instabilities develop. We can thus neglect effects introduced by the boundary conditions.

B. Intermediate time t = 500

The electron and proton phase space density distributions $f_e(r, v_r)$ and $f_p(r, v_r)$ at the time $t = 500$ are shown in Fig. 5. The majority of the electrons in Fig. 5(a) is confined by the immobile positive charge background in the interval $r < 0.95 r_W$. Their phase space density and the characteristic electron speed decrease drastically at $r \approx r_W$ but remain relatively high up to $r \approx 1.5 r_W$. The phase space density decreases by another two orders of magnitude as we go to even larger radii. The radial interval $1 < r/r_W < 1.5$ with the elevated electron phase space density and mean speed coincides with the radial interval that is occupied by the distribution of mobile protons. An almost closed circular proton phase space structure is present at $r \approx 1.03 r_W$ in Fig. 5(b) that is sustained by a local excess of negative charge. The profile of the proton phase space density distribution in Fig. 5(b) increases linearly with the radius for $r > 1.05 r_W$, which is characteristic for a rarefaction wave. The protons reach a peak speed $\approx 200 v_p$, which is comparable to $v_e/10$ and about the same as that in Ref. 11. Only a small fraction of the protons reaches this speed, which limits the loss of electron thermal energy at this time (see Fig. 2). The low electron phase space density for $r > 2 r_W$ implies that all electron processes close to the boundary are slow and do not carry much energy.

The densities of the mobile particle species at $t = 500$ are shown in Fig. 6. They are obtained from the integration of the phase space densities in Fig. 5 over v_r. They are normalized to their initial value. The electron density decreases by an order of magnitude close to the boundary of the immobile positive charge background at $r = 0.95 r_W$. It increases again for $r > r_W$ and reaches a local maximum at around $r \approx 1.15 r_W$, close to the peak of the mobile proton's density. Both densities decrease gradually beyond this radius. The proton density falls off steeply at its front at $r \approx 1.5 r_W$ (see also Fig. 5(b)).

Figure 7 shows the in-plane electric field distribution at $t = 500$. The electric field modulus shows a more complex pattern than at the earlier time. The electric field peaks at $r \approx r_W$, and it is sustained by the electron density gradient close to the boundary of the immobile positively charged

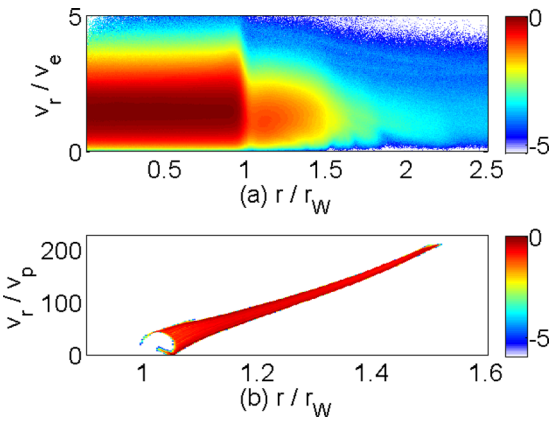

FIG. 5. The 10-logarithmic phase space densities $f_e(r, v_r)$ of the electrons (a) and $f_p(r, v_r)$ of the protons (b). The densities are normalized to their initial value. The simulation time is $t = 500$.

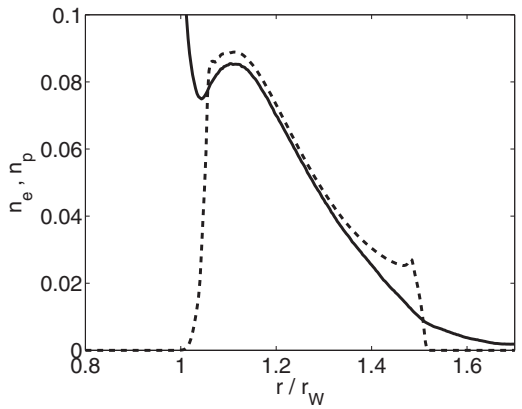

FIG. 6. The electron density $n_e(r)$ and the proton density $n_p(r)$ (dashed curve) sampled at the time $t = 500$ and normalized to the respective initial density values.

background at $r = 0.95r_W$. The electric field modulus goes through a minimum at a slightly larger radius. The reason for this radial oscillation is that we have two regions with an excess of positive charge, which are separated by a radial interval with a negative excess charge at $r \approx r_W$ (see Fig. 6). An electric field with a significant amplitude modulus that extends over a large radial interval is observed at $1.1 < r/r_W < 2$. The electric field modulus in this band peaks at $r \approx 1.5r_W$, which coincides with the front of the proton distribution in Fig. 6. It thus corresponds to the ambipolar electric field driven by this density gradient, and it decreases for larger radii where we only find electrons. The electric field modulus reaches its minimum at $r \approx 2r_W$.

Figure 8 displays the distribution of B_z at $t = 500$. We observe a strong localized magnetic field structure. Its amplitude peaks at $r \approx 0.8r_W$ and it decreases as we go to $r \approx r_W$ and beyond. The amplitude oscillates once in the azimuthal direction and the associated wavelength $\lambda_\rho \approx 2\pi r_W$ is thus much larger than the one in the radial direction, which we can estimate as follows. We find a magnetic field maximum at $x \approx -0.3r_W$ and $y \approx 0.3r_W$ and a minimum at $x \approx -0.6r_W$ and $y \approx 0.6r_W$. The wavelength of the radial oscillation is thus $\lambda_r \approx 0.5r_W$. The magnetic amplitude outside this radial interval is at noise levels. The magnetic noise is distributed over the entire simulation box, while the magnetic structure

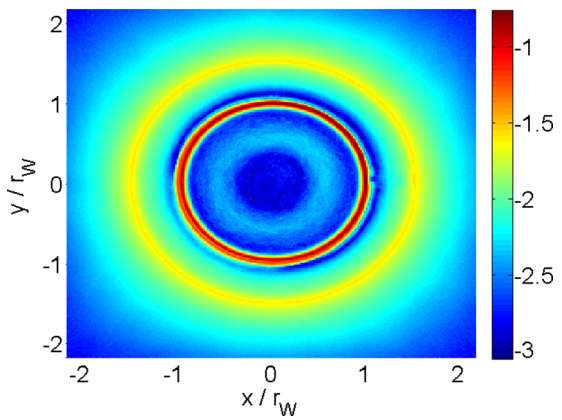

FIG. 7. The 10-logarithmic modulus of the electric field $|E_p(x, y)|$ sampled at the time $t = 500$.

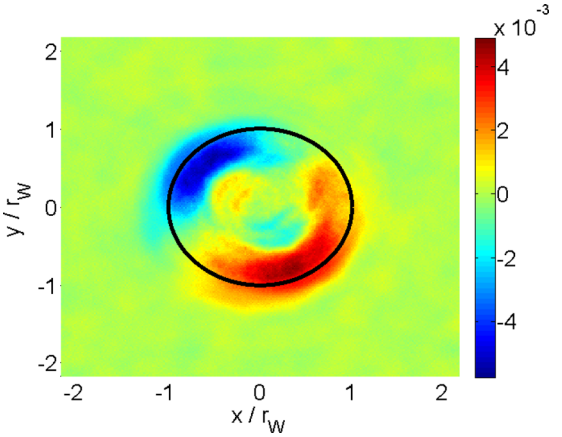

FIG. 8. The magnetic field amplitude $B_z(x, y)$ sampled at the time $t = 500$. Overplotted is a circle of radius $r = r_W$ (enhanced online) [URL: http://dx.doi.org/10.1063/1.4769128.3].

is localized in a small radial interval. This explains why we do not observe a more pronounced growth of the magnetic field energy in Fig. 2(d).

It is instructive to compare the radial interval, in which the magnetic field grows, with the one that shows a thermal anisotropy. We determine for this purpose the thermal energy densities of the electrons in the radial and azimuthal directions. We consider only the in-plane component of the speed $\mathbf{v}_{p,j} = (v_x, v_y)_j$ of the jth computational electron. The radial component of the thermal energy $K_{r,j} = v_{r,j}^2$ is computed from the projection $v_{r,j} = \mathbf{v}_{p,j} \cdot \mathbf{r}_j / r_j$, where $\mathbf{r}_j$ is the position vector of the electron in circular coordinates, and $K_{\rho,j} = v_{p,j}^2 - K_{r,j}$. The partial thermal energies and the anisotropy A are then obtained from the summations

$$K_r(i\delta_r) = \sum_{j=1}^{N_e} K_{r,j}\delta_{i,j}, \tag{5}$$

$$K_\rho(i\delta_r) = \sum_{j=1}^{N_e} K_{\rho,j}\delta_{i,j}, \tag{6}$$

$$A = K_r/K_\rho, \tag{7}$$

where $\delta_{i,j} = 1$, if $(i-1)\delta_r \le r_j < i\delta_r$ and zero otherwise. The width of a radial bin $\delta_r = \Delta_x$. We thus obtain a histogram $A(i)$ of the radial distribution of the thermal anisotropy. The anisotropy $A(r)$ is compared with the magnetic energy

$$P_{Bz}(n\delta_r) = (\Delta_x^3/2\mu_0)\sum_{i,j=1}^{N_g} B_z^2(i - N_g/2, j - N_g/2)\delta_{i,j,n}, \tag{8}$$

where $\delta_{i,j,n} = 1$ if $I((i - N_g/2)^2 + (j - N_g/2)^2) = n^2$, with I being a round-off operation. This azimuthal integration, rather than the azimuthal average, emphasizes magnetic fields at larger radii.

Figure 9 demonstrates that the magnetic field starts to grow at $t \approx 200$, when an anisotropy $A(r) < 1$ has formed that is sufficiently strong and wide. The magnetic field grows initially in the interval $0.7 < r/r_W < 1.1$ but it expands later on in both radial directions. Its front reaches $r \approx 1.5r_W$ at

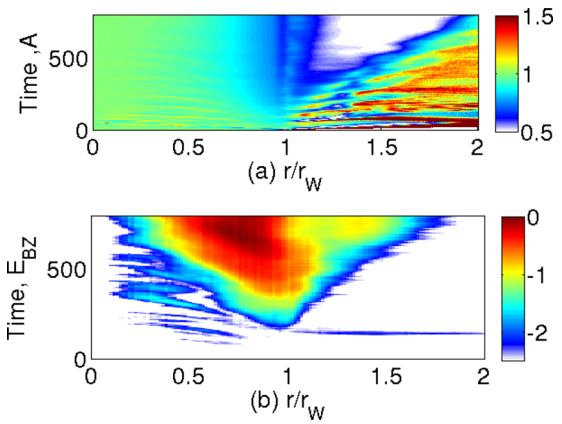

FIG. 9. The ratio A between the mean radial energy and the mean perpendicular energy of electrons is shown on a linear color scale in (a). The spatio-temporal evolution of the magnetic energy density is shown on a 10-logarithmic color scale in (b).

$t = 500$, which coincides with the tip of the proton distribution in Fig. 6. It is thus confined to within the rarefaction wave. The radial interval where $P_{BZ} \approx 1$ is initially stationary but the magnetic field distribution changes after $t \approx 500$. What appears to be a sidelobe develops at $r \approx 1.4 r_W$. This change takes place on a few tens of ω_p^{-1}. The plasma frequency in the rarefaction wave is about $\omega_p/4$ at $t = 500$ (see Fig. 6) and the growth time of the sidelobe is thus faster than that expected from any instability. Indeed, the on-line enhancement of Fig. 8 shows that the magnetic B_z-field leaks out from within the cloud into the rarefaction wave.

C. Late time t = 800

Figure 10 shows its distribution at $t = 800$. The extrema of B_z are located within $r = r_W$, and the amplitude of B_z is constant as a function of r for $1 < r/r_W < 1.5$. The peak of the normalized magnetic amplitude at the saturation time of the instability is $\approx 7 \times 10^{-3}$ and thus about 50% of the one observed in Ref. 11. The peak magnetic energy density is thus significantly lower in the present simulation. The magnetic energy has been confined to within $r \approx r_W$ until $t \approx 600$, and it forms a TM mode until then (see Fig. 8). The rapid expansion of the magnetic energy after $t \approx 600$ implies that this TM mode suddenly expands.

We can understand the circular plasma cloud as the cross section of a cylindrical waveguide with an axis that is aligned with z. The expansion of the mobile protons implies that the radius of the cross-section of this waveguide increases in time. It is well-known that changes in the radius of a waveguide induce a coupling of TM and TE modes.[20] The magnetic field of a TE mode would be oriented in the simulation plane.

Figure 11 evidences that a TE wave is indeed present at $t = 800$. A structure is visible in the distribution of the in-plane magnetic field $B_p = (B_x^2 + B_y^2)^{1/2}$. It is located in the same radial interval as the magnetic field of the TM mode. The magnetic field patterns in B_z and B_p have the same azimuthal wave number and both are phase-shifted by 90° relative to each other. The magnetic energy of the TE mode grows after $t = 800$ to values exceeding that of the TM wave (not shown). We do not discuss the evolution for $t > 800$. The TE wave expands out to the boundaries shortly after this time, which results in finite box effects, while the TM wave remains confined by the rarefaction wave as discussed previously.[11]

The different behaviour of the TM and TE modes can be explained by the different plasma response to their electric fields in our 2D box geometry. An electric field orthogonal to the simulation box plane cannot result in charge density modulations, since we do not resolve the z-direction. It, thus, only affects the current distribution. An in-plane electric field does, however, modulate also the charge density. The dilute electron plasma between the front of the rarefaction wave and the boundaries cannot support strong charge density waves but it can easily support the large currents from the TE wave and the latter can expand more easily.

IV. DISCUSSION

We have modeled here with a 2D PIC simulation the expansion of a circular plasma cloud into a vacuum, which has been driven by the thermal pressure of the electrons. It is a follow-up study of a previous simulation experiment. It

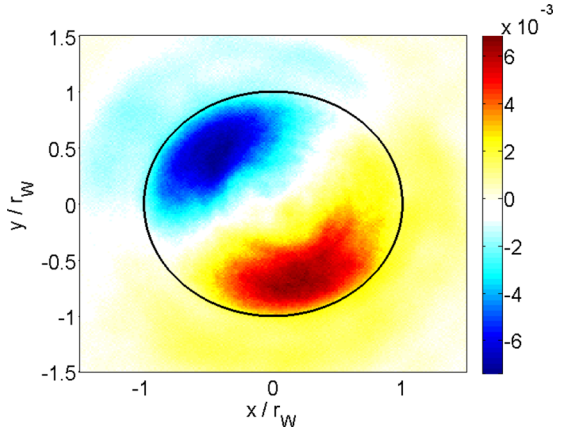

FIG. 10. The magnetic field amplitude $B_z(x, y)$ sampled at the time $t = 800$. Overplotted is a circle of radius $r = r_W$.

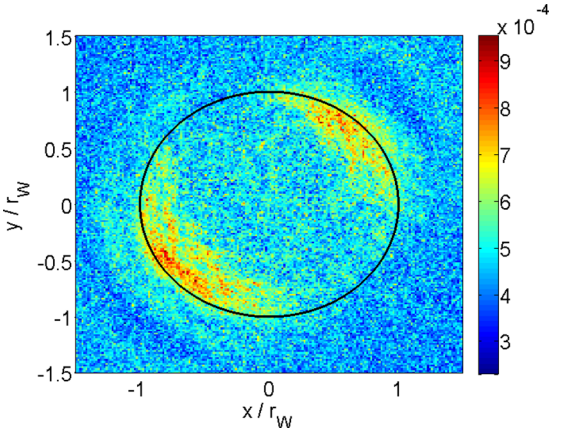

FIG. 11. The magnetic field amplitude $|B_p(x, y)|$ sampled at the time $t = 800$. Overplotted is a circle of radius $r = r_W$ (enhanced online) [URL: http://dx.doi.org/10.1063/1.4769128.4].

aimed at explaining the growth of magnetic fields in the rarefaction wave, which is generated by the ablation of a wire by a laser pulse.[10] It considered the expansion of a circular plasma cloud, which consisted of spatially uniform hot (32 keV) electrons and cool (10 eV) protons. Here, we have confined the mobile protons to the border of the plasma cloud. This hollow ring distribution is a more accurate approximation of the experimental conditions. The rarefaction wave observed in Ref. 10 contains primarily the light ions from the surface impurities, which have been ionized by the strong surface electric field and current.[18] However, computational constraints require us to represent here the electrons as a hot (32 keV) species that is uniformly distributed over the entire plasma cloud. The electrons in the experiment reach MeV temperatures but they are confined to the wire's surface. Choosing cooler electrons reduces the difference between the electron and proton Debye lengths, which is computationally efficient, while it ensures that the thermal energy that drives the expansion is comparable in simulation and experiment.

Our results are as follows. The ambipolar electric field driven by the electron's thermal expansion results in the formation of a rarefaction wave. The fastest protons reach a speed that is comparable to about a tenth of the electron thermal speed, which equals the value observed in Ref. 11. The proton acceleration is thus not affected by the choice of the initial proton distribution. However, the density of the rarefaction wave is limited by the number of available mobile protons. The spatially uniform proton distribution in Ref. 11 provided a continuous feed of mobile protons, while the number of mobile protons we introduce here is limited. The plasma density in the rarefaction wave is thus lower than that in Ref. 11. The lower plasma frequency implies a slowdown of the instabilities in the rarefaction wave.

Although the thermal anisotropy in the electron distribution here and in Ref. 11 has been comparable, the Weibel-type instability could apparently not develop in the rarefaction wave during the simulation time. This instability started instead in the dense core of the plasma cloud and the magnetic field diffused out into the rarefaction wave. The simulation has shown that the magnetic instability driven by the thermal anisotropy is robust against significant changes in the initial conditions, which is important with respect to magnetic field growth in turbulent astrophysical plasma.

The present simulation sheds light on the mechanism by which the in-plane magnetic fields grew in Ref. 11. A TE mode can probably not be driven by a plasma instability. The electromagnetic forces and the plasma flow are confined to within the simulation plane. No current can thus develop in the orthogonal direction. Orthogonal plasma currents are, however, needed to maintain the in-plane magnetic field. The present simulation hints at wave-wave coupling as the cause to the TE wave. The plasma in the radial interval $r < 0.95r_W$ with the immobile positive charge background is equivalent to a cylindrical waveguide, and the thermal anisotropy of the electrons results in the growth of a TM wave inside the wave guide. The plasma of the dilute rarefaction wave is a perturbation of the waveguide's cross section. A varying radius of a waveguide can couple TM and TE modes.[20] Here, this coupling results in the growth of in-plane magnetic fields. A wave coupling between a TM and a TE wave drives orthogonal electric fields, which can accelerate electrons in this direction. Future work will address this wave coupling with a larger simulation box. The evolution of the TE wave can then be examined for a longer time without finite box effects.

ACKNOWLEDGMENTS

M.E.D. thanks Vetenskapsrådet (Grant 2010-4063) and G.S. thanks the Leverhulme foundation (Grant ECF-2011-383) for financial support. Computer time and support has been provided by the HPC2N computer center in Umeå, Sweden.

[1]D. A. Tidman and R. A. Shanny, Phys. Fluids **17**, 1207 (1974).
[2]K. M. Ferriere, Rev. Mod. Phys. **73**, 1031 (2001).
[3]H. J. Volk, E. G. Berezhko, and L. T. Ksenofontov, Astron. Astrophys. **433**, 229 (2005).
[4]A. R. Bell, Mon. Not R. Astron. Soc. **353**, 550 (2004).
[5]J. Niemiec, M. Pohl, T. Stroman, and K. Nishikawa, Astrophys. J. **684**, 1174 (2008).
[6]T. Grismayer, P. Mora, J. C. Adam, and A. Heron, Phys. Rev. E **77**, 066407 (2008).
[7]C. Thaury, P. Mora, A. Heron, and J. C. Adam, Phys. Rev. E **82**, 016408 (2010).
[8]G. Sarri, M. E. Dieckmann, I. Kourakis, and M. Borghesi, Phys. Rev. Lett. **107**, 025003 (2011).
[9]G. Sarri *et al.*, New J. Phys. **13**, 073023 (2011).
[10]K. Quinn *et al.*, Phys. Rev. Lett. **108**, 135001 (2012).
[11]M. E. Dieckmann, G. Sarri, G. C. Murphy, A. Bret, L. Romagnani, I. Kourakis, M. Borghesi, A. Ynnerman, and L. O'C. Drury, New J. Phys. **14**, 023007 (2012).
[12]A. Bret, L. Gremillet, and M. E. Dieckmann, Phys. Plasmas **17**, 120501 (2010).
[13]E. Weibel, Phys. Rev. Lett. **2**, 83 (1959).
[14]R. L. Morse, and C. W. Nielson, Phys. Fluids **14**, 830 (1971).
[15]L. Palodhi, F. Califano, and F. Pegoraro, Plasma Phys. Controll. Fusion **51**, 125006 (2009).
[16]A. Stockem, M. E. Dieckmann, and R. Schlickeiser, Plasma Phys. Controll. Fusion **51**, 075014 (2009).
[17]A. Stockem, M. E. Dieckmann, and R. Schlickeiser, Plasma Phys. Controlled Fusion **52**, 085009 (2010).
[18]K. Quinn *et al.*, Phys. Rev. Lett. **102**, 194801 (2009).
[19]D. A. Tidman and L. L. Burton, Phys. Rev. Lett. **37**, 1397 (1976).
[20]T. U. Haq, K. J. Webb, and N. C. Gallagher, IEEE MTT-S Int. Microwave Symp. Dig. **3**, 1613 (1995).
[21]J. M. Dawson, Rev. Mod. Phys. **55**, 403 (1983).
[22]J. W. Eastwood, Comput. Phys. Commun. **64**, 252 (1991).